The University of Tehran Press

Pollution

Print ISSN: 2383-451X
Online ISSN: 2383-4501

https://jpoll.ut.ac.ir/

Application of Artificial Neural Network and Multiple Linear Regression for Modelling Adsorptive Removal of Pb (II) ions over *Cedrus deodara* Bark Powder

Anurag Samson Lall[1]✉ | Avinash Kumar Pandey[2] | Jyoti Vandana Mani[1]

1. Department of Chemistry, Sam Higginbottom University of Agriculture, Technology and Sciences, Prayagraj, Uttar Pradesh, 211007, India.
2. Department of Chemistry, GLA University, Chaumuhan, Mathura, Uttar Pradesh, 281406, India.

Article Info

Article type:
Research Article

Article history:
Received: 17 September 2023
Revised: 22 October 2023
Accepted: 8 December 2023

Keywords:
ANN
MLR
Adsorption
Cedrus deodara
lead

ABSTRACT

Cedrus deodara is a coniferous tree native to Himalayan region. Its wood is a valuable resource for the timber industry; however, its bark is typically discarded as a waste material. The present study examines the performance of Cedrus deodara bark powder (CD) as an inexpensive adsorbent for elimination of Pb (II) ions. In addition to this multiple linear regression (MLR) and artificial neural network (ANN) models were developed for modelling the adsorption process and prediction of Pb (II) removal efficiency. The structural and chemical properties of CD were explored using Field Emission Scanning Electron Microscope (FE-SEM), Energy Dispersive Spectrometer (EDS), X-Ray Diffractometer (XRD) and Fourier Transform Infrared Spectroscopy (FTIR). Batch experiments were conducted to investigate the influence of factors including pH, contact time, initial Pb (II) concentration and temperature on Pb (II) adsorption. The adsorption followed pseudo-second-order kinetic and Langmuir isotherm models with maximum monolayer uptake capacity 77.52 mg/g. Based on the thermodynamic criteria, the process was endothermic and spontaneous with enthalpy change (ΔH = 8.08 kJ/mol), free energy change (ΔG = -2.44 kJ/mol) and entropy change (ΔS = 0.03 kJ/K/mol). Statistical comparison of MLR model (R2 = 0.817, RMSE = 8.954, MAPE = 17.379 %) and ANN model (R2 = 0.993, RMSE = 1.777, MAPE = 2.054 %) confirmed that ANN model was far more accurate in predicting removal efficiency.

Cite this article: Lall, A.S., Pandey, A. K., & Mani, J. V. (2024). Application of Artificial Neural Network and Multiple Linear Regression for Modelling Adsorptive Removal of Pb (II) ions over Cedrus deodara Bark Powder. *Pollution*, 10 (1), 528-549.
https://doi.org/10.22059/POLL.2023.365500.2076

 Publisher: The University of Tehran Press.
DOI: https://doi.org/10.22059/POLL.2023.365500.2076

INTRODUCTION

Pure and uncontaminated water is an indispensable resource for supporting life on Earth. However, as the global industrialization continues to accelerate, the quality of natural water resources is unprecedentedly deteriorating due to the rising levels of pollutants. A diverse array of contaminants, both synthetic and natural, have entered the surface and ground water, posing imminent risk to the human health and natural environment. The worldwide scientific communities recognize heavy metals as contaminants of principal concern on account of their elongated environmental persistence and substantial toxicity. Several studies indicate that heavy metals like Zn, Cr, Pb, Ni, Cu, and Cd are primarily present in different water bodies across the world (Banerjee *et al.,* 2016). Various industrial, agricultural, and domestic operations allow these metals to infiltrate water bodies, where they eventually contaminate them.

Due to its ubiquitous prevalence and adverse health impacts, lead, a well-known heavy

*Corresponding Author Email: *anuragsam7son@gmail.com*

metal contaminant, has received considerable attention. The Agency for Toxic Substances and Disease Registry (ATSDR) has ranked lead as a rank 2 contaminant in their Substance Priority List 2019 (ATSDR, 2019). According to World Health Organization (WHO), lead is amongst the metals of greatest concern due to its potentially toxic nature and tendency to diffuse throughout the body, inflicting deleterious health effects. Exposure to lead contamination is known to cause serious neurological abnormalities, developmental delays, and cognitive diseases, therefore it can cause serious health repercussions, especially for children and pregnant women.

Due to the profound consequences of heavy metal exposure, a variety of remediation methods have been adopted to eliminate these contaminants from water. The frequently employed procedures include, membrane separation, chemical precipitation, electrocoagulation, ion exchange and adsorption. Although each of these strategies has advantages and disadvantages, the adsorption technique has shown to be the most efficient way to remove heavy metals due to its cheap cost, adaptability, and high efficiency (Barakat, 2011; Ciesielczyk *et al*., 2013; Carolin *et al*., 2017).

Due to environmental and economic factors, biomass from agricultural leftovers such as rice husk, wheat husk, gram husk, peanut shell, walnut shell, soybean hulls, cotton stalks, and bark from various trees has garnered substantial interest as adsorbents (Sud *et al*., 2008; Fomina & Gadd, 2014; Haydar *et al*., 2020). Because of its distinctive morphological and chemical properties, tree bark, a commonly available waste material generated by forestry and horticulture processes, has demonstrated extraordinary adsorption qualities (Vazquez *et al*., 2002; Liang *et al*., 2014; Sen *et al*., 2015). It often contains a wide range of chemical components such as cellulose, hemicellulose, lignin, and a variety of extractives that vary depending on the species of tree. Numerous functional groups, including carboxyl and hydroxyl groups, can be easily found in tree bark which may readily bind with metal ions present in water (Liang *et al*., 2014). *Cedrus deodara* is a cedar tree species native to the Himalayan area, which particularly includes India, Pakistan, and Nepal (Jain *et al*., 2015). It is an evergreen tree noticed for its massive size, conical structure and fragrant leaves. Its wood is commonly used in construction, particularly for the crafting of doors, windows, and furniture, due to its longevity and resistance to decay (Grover, 2021). Since the bark portion is typically discarded by the wood processing industries, it may be utilized possibly as a lucrative sorbent for eliminating heavy metal ions.

Computational techniques including Artificial neural networks (ANN) and Multiple linear regression (MLR) have recently been employed as exceptionally effective and versatile approaches for mathematical modelling of a wide range of processes (Zhang *et al*., 2017; Taoufik *et al*., 2021). Typically, the basis behind these techniques is to use the experimental data to ascertain a functional relationship between the independent operational variables and the dependent response variable. Therefore, the objective of the present study is to determine the potential of *Cedrus deodara* tree bark powder for the adsorptive elimination of Pb (II) ions and to analyze the effectiveness of MLR and ANN models for modelling the adsorption process and prediction of Pb (II) removal efficiency.

MATERIALS AND METHODS

Analytical grade consumables utilized in the present investigation were purchased from E. Merck, India Ltd. A stock solution containing 1000 ppm Pb (II) was generated by dissolving accurately measured 1.60 g of Pb $(NO_3)_2$ (99.95% Assay) in 1 litre of acidified double distilled water. *Cedrus deodara* tree bark was procured from Pauri, Uttarakhand, India (30° 8' 53.6388'' N, 78° 46' 16.3056'' E). The acquired bark pieces underwent thorough cleansing with distilled water, dried in the sun and then chopped into smaller chunks. These chunks were then fully air-dried in hot air oven with temperature set to 110°C. The obtained material was then finely grinded to create a powder with 90 – 125 μm sized particles. To prevent unnecessary colour

release in aqueous media, the water-soluble tannins and other constituents were eliminated by periodically boiling 30 g of bark powder in 250 ml of double-distilled water, followed by decanting, until no further colour discharge was noticed (Reddy *et al*., 2011; Das *et al*., 2020). The final product was then dried out within a hot air furnace at 80°C, then cooled to room temperature and stored as the adsorbent *Cedrus deodara* bark powder (CD) in air tight plastic bottles.

For conducting batch adsorption experiments 1000 ppm standard solution of Pb (II) was diluted to prepare solutions having concentrations within the range 10 – 250 ppm. Separate measurements of CD were held in conical flasks that carried 200 ml of Pb (II) solutions having required concentrations. 0.1M HCl and 0.1M NaOH solutions were added for altering the pH of the solutions in each of these flasks. These flasks were subsequently placed in an orbital shaker at an appropriate temperature, maintained at 140 rpm speed. Batch tests were performed by varying a variety of variables including pH, adsorbent dose, initial Pb (II) concentration, contact time and temperature. Finally, the mixtures were made to pass through Whatman filter paper and Pb (II) concentration in the filtrate was evaluated using Atomic Absorption Spectrophotometer (Analytic Gena, Model AAS 5EA) with hollow cathode lamps at characteristic wavelength of 217 nm (CWC, 2019).

Following equations were utilized to compute the removal efficiency (R%) and the uptake capacity (Q_t) at any given time t (Mittal *et al*., 2016 a; b):

$$Q_t = \frac{(C_0 - C_t)x\ V}{W}$$

$$R\% = \frac{(C_0 - C_t)x\ 100}{C_0}$$

C_0 and C_t are the initial and final concentrations of Pb (II) ion measured at time t. The volume of solution (l) was denoted by V, while W signified the adsorbent mass (g). The collected data was evaluated utilizing suitable kinetic and isotherm models.

After Pb (II) adsorption, the alterations in surface texture and elemental distribution of CD were inspected by FE-SEM (JEOL JSM – 7610F with Smart Au Sputter Coater) (Pradhan *et al*., 2018; Kumar *et al*., 2019). During the procedure, a focused electron beam with a 30kV accelerating voltage and a 200 nA probe current was used. An EDS (Oxford EDS Liquid Nitrogen free) detector for backscattered electrons was connected to the apparatus. The functional groups across the adsorbent surface were determined using FTIR (Perkin Elmer - Spectrum Two with DTGS Detector). The equipment used KBr optics, which had a sensitivity ratio of 32000:1 and a resolution of 1 cm^{-1} (Litefti *et al*., 2019). The X-Ray Diffractometer (Model: Bruker D8 Advance) was deployed to evaluate the alerations in the crystallographic and micro structural characteristics of CD after Pb (II) loading within the region $2\theta = 5°$ to 90° with a scan speed set at 10°/ min employing Cu Kα wavelength $\lambda = 1.54$ Å (Kumar *et al*., 2018; 2020). The notable peaks observed via XRD analysis were identified and assigned using the program PANalytical X'Pert HighScore Plus 3.0.

The collected experimental data was utilised to generate adequate mathematical models for analysing the intricate adsorption process and predicting Pb (II) removal efficiency (R%) using multiple linear regression (MLR) and artificial neural network (ANN). The purpose of the MLR and ANN models was to examine the mathematical relationship between the response variable (R%) and the predictor variables including pH, adsorbent dosage (g), contact time (min), initial concentration (mg/l), and temperature (°C). The MLR model was formulated with help of software Minitab Version 21.1.0 (Minitab LLC, Chicago, USA). The approach was

based on fitting the obtained adsorption data to a linear equation. Following equation was used for formulating the model:

$$y = \beta_0 + \beta_1 x_1 + \beta_2 x_2 + \beta_3 x_3 + ... + \beta_n x_n$$

where y is the response variable and β_0 is the y-intercept while β_1, β_2, β_3,…., β_n represent the coefficients for the predictor variables x_1, x_2, x_3,….., x_n respectively. The significance of these predictor variables and the overall MLR model in predicting the response variable was investigated with help of analysis of variance (ANOVA) results.

Artificial neural networks (ANNs) are digital representations of the intricate structure and functioning of the human nervous system and brain. ANNs can easily comprehend any arbitrary mathematical function with great precision and they do not require highly regulated experimental setups (Kareem & Pathak, 2016). ANNs usually have layered structure consisting of interlinked nodes. The network may be classified as 'single-layered' or 'multi-layered' based upon the number of layers. Single-layered networks have only input and output layers. While multi-layered networks have certain number of hidden layers of nodes for further computational processing in order to recognise the data patterns and acquire a better comprehension of data (Sazli, 2006). In general, the nodes and the inter-connections between them represent the biological structure of neurons and the branching dendrites respectively (Hallinan, 2013). Each node takes information as input from other nodes present in previous layer, analyses it, and then transmits the results to other nodes in subsequent layer. Therefore, the output of a particular node depends on the weighted sum of the inputs provided by the nodes in previous layer. Consider node j present in the hidden layer connected to the node i of input layer via synaptic weight $w_{i,j}$. If the output at node i is represented by v_i, the resultant output value at node j may be expressed as follows (Hallinan, 2013):

$$v_j = \sum_{i=1}^{n} v_i . w_{i,j}$$

This value is further mathematically transformed using a non-linear activation function so as to ensure compliance of boundary conditions. This generated output is then fed as input to the subsequent layer of nodes. This network architecture thus obtained may then be employed to recognize the mathematical dependence of response variable on predictor variables. In order to ensure lower rates of error, the network training was accompanied by Levenberg-Marquardt algorithm. This involves fine-tuning the synaptic weights at each successive iteration by minimizing the sum of square errors between the target values and predicted values of response variable (Lee & Choi, 2013; Syahrullah & Sinaga, 2016). The 'nnstart' function of the MATLAB software version R2018a (MathWorks, Massachusetts, USA) was employed to develop the ANN model for this investigation.

The accuracy and the quality of MLR and ANN models in predicting the adsorptive removal (R%) were estimated and compared in terms of coefficient of determination (R^2), root mean square error (RMSE) and mean absolute percentage error (MAPE) which were computed using following equations (Yetilmezsoy & Demirel, 2008; Xie *et al*., 2022):

$$R^2 = 1 - \frac{\sum_{i=1}^{n} (y_{i,obs} - y_{i,pred})^2}{\sum_{i=1}^{n} (y_{i,obs} - y_{mean,obs})^2}$$

$$RMSE = \left[\frac{\sum_{i=1}^{n} \left(y_{i,obs} - y_{i,pred} \right)^2}{n} \right]^{1/2}$$

$$MAPE = \frac{1}{n} \sum_{i=1}^{n} \left[\frac{y_{i,obs} - y_{i,pred}}{y_{i,obs}} x100 \right]$$

where n = total number of observations, while $y_{i,obs}$ and $y_{i,pred}$ represent the experimentally observed and model predicted values corresponding to i^{th} observation respectively. Similarly $y_{mean,obs}$ denotes the mean value of all experimental observations. The accuracy of prediction for a particular model may be demonstrated by higher R^2 value and lower values of RMSE and MAPE (Kulisz *et al*., 2021). Usually, MAPE value lower than 10% indicates excellent predictive accuracy of the model (Xie *et al*., 2022)

RESULTS AND DISCUSSION

The FE-SEM micrographs of adsorbent CD before and after loading Pb (II) ions and corresponding EDS spectra have been presented in **Figure 1**. It is evident from figure that the surface of CD was uneven and rough surface with irregular and sharp edges. It also revealed a number of asymmetrical cavities present throughout the surface. The loading of Pb (II) ions partially filled the surface cavities, and the rough, jagged edges were substantially rounded. As

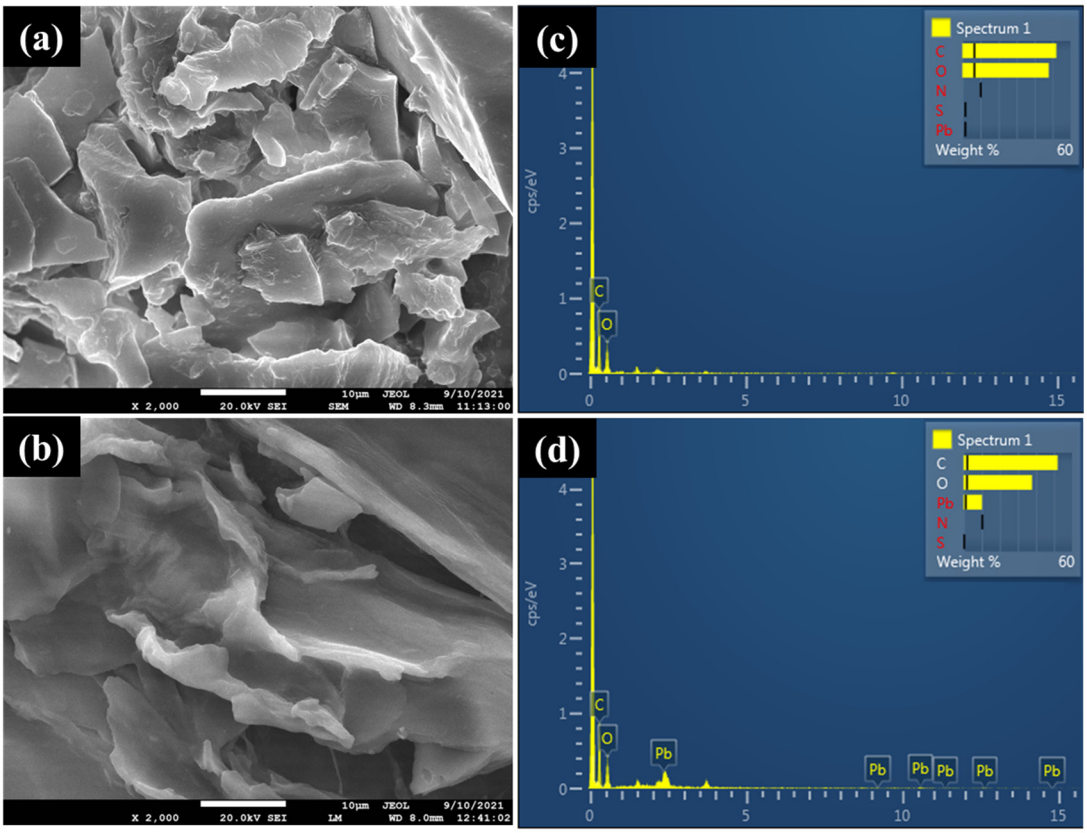

Fig. 1. FE-SEM images of CD (a) before and (b) after Pb (II) adsorption; EDS spectra of CD (c) before and (d) after Pb (II) adsorption

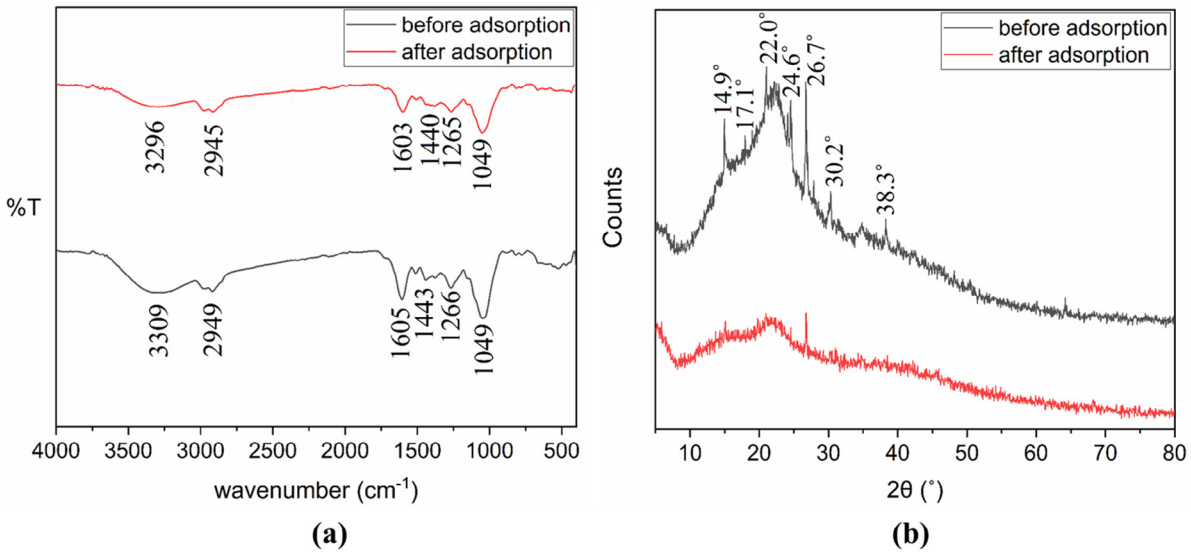

Fig. 2. (a) FTIR and (b) XRD spectra of CD before and after Pb (II) adsorption.

a result, CD surface became noticeably smoother. On examining the EDS spectra of CD, the elemental lines were only observed for carbon and oxygen. Accordingly, CD was comprised mainly of carbon (52.13% w/w) and oxygen (47.87% w/w). The EDS spectra of CD after Pb (II) adsorption revealed characteristic lines for Pb (Mα), Pb (Lα) and Pb (Lβ) at 2.3, 10.5 and 12.6 keV respectively (Ijomah & Okoyeh, 1988; Capobianco *et al*., 2018). Consequently, the overall elemental composition of the adsorbent was also altered, with distribution of the elements as carbon (52.06% w/w), oxygen (37.77% w/w) and lead (10.17% w/w) respectively.

Figure 2 (a) displays the FTIR spectra of CD before and after loading of Pb (II) ions. The FTIR spectra of CD before Pb (II) adsorption demonstrated distinct peaks at 3309 and 1049 cm^{-1} which could be assigned to the O-H stretching (Hwang *et al*., 2018) and C-O stretching (Teshager *et al*., 2022) frequencies for alcohol respectively. Moreover, the existence of a peak at 1266 cm^{-1} may indicate the C-O stretching frequency for alkyl aryl ethers (Coates, 2000). Also, the peaks at 1605 and 1443 cm^{-1} may be assigned to the conjugated C=C and C=C-C bonds in aromatic ring structure, thereby revealing the presence of lignin (Wu *et al*., 2019). The peak at 2949 cm^{-1} is most likely related to the methyl C-H stretching (Fuks *et al*., 2006). The adsorption of Pb (II) ions induced a change in peak frequencies as well as an overall drop in peak intensities. The O-H stretching unveiled a major shift from 3309 to 3296 cm^{-1} reflecting involvement of O-H group in adsorption. The absorptions at 1605 and 1443 cm^{-1} also displayed a shift to lower frequencies 1603 and 1440 cm^{-1} respectively, revealing a possible interaction of π electrons with the metal ions (Wu *et al*., 2019). Similarly, the peaks at 2949 and 1266 shifted to lower frequencies 2945 and 1265 cm^{-1} respectively. Therefore, the FTIR data suggested that the hydroxyl groups of lignin, cellulose, and hemicellulose participated in the adsorption process (Politi & Sidiras, 2020).

The XRD spectra of CD before and after loading of Pb (II) ions has been shown in Figure 2 (b). Major diffraction peaks for CD were observed at positions 2θ = 14.9°, 17.1°, 22.0°, 24.6°, 26.7°, 30.2° and 38.3°. The presence of cellulose I may be easily identified by the broad hump along the region 2θ = 15° and 25° (Liang *et al*., 2018; Shooto *et al*., 2020). Diffraction peaks at 2θ = 24.6°, 26.7° and 30.2° may indicate the existence of p- coumaric acid, matching with the JCPDS card no. 00-037-1722. Earlier studies confirmed the occurrence of major sterol extractives in Cedrus deodara stem bark including stigmasterol and ß- sitosterol (Hafizoğlu & Holmbom, 1987). Accordingly, the peaks at 2θ = 26.7° and 30.2° may also be ascribed to

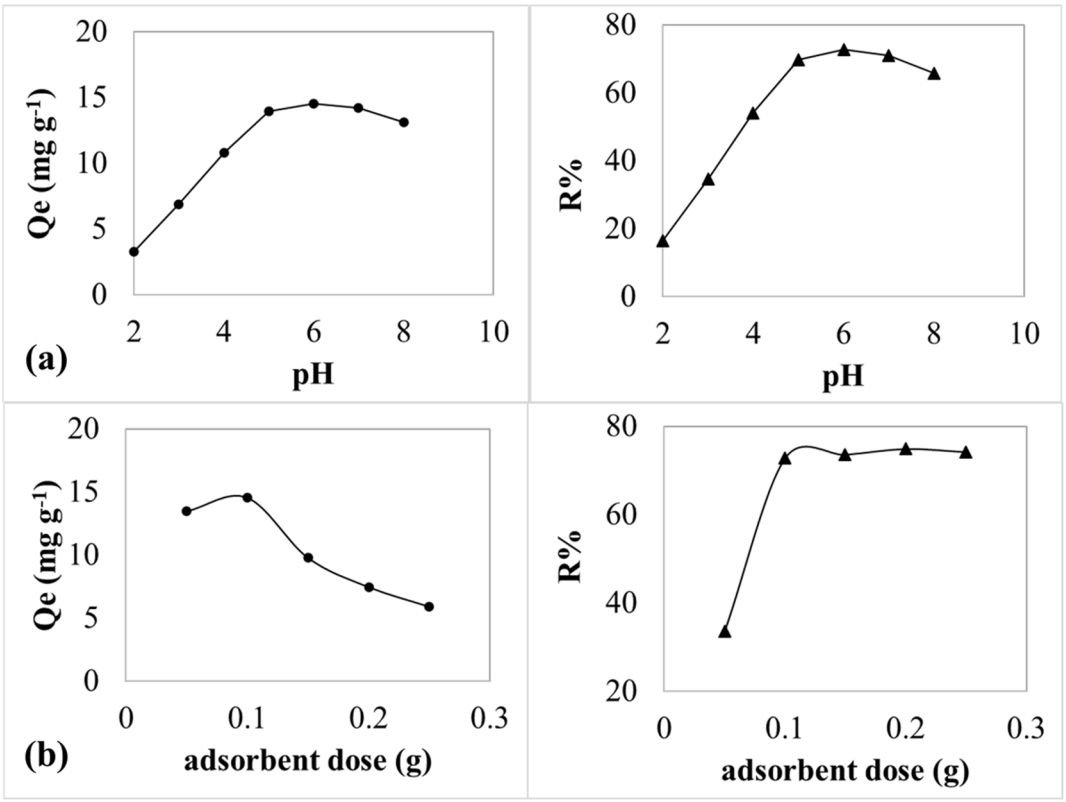

Fig. 3. (a) Effect of pH and (b) adsorbent dose on adsorption of Pb (II) over CD

ß- sitosterol (JCPDS card no. 00-010-0641). In a similar way, peaks at 2θ = 24.6° and 38.3° are attributable to the presence of stigmasterol (JCPDS card no. 00-029-1925). It is noteworthy that the peak positions of CD before and after Pb (II) loading were identical, with the exception that the peak intensities were considerably lowered. This undoubtedly demonstrates that the adsorption process comprised physisorption of Pb (II) over the CD surface (Srivastava *et al*., 2017; Gupta & Mondal, 2020).

Figure 3 illustrates the effect of change in pH and adsorbent dose on equilibrium uptake capacity (Q_e). For examining the effect of pH, batch tests were performed using 0.1 g of CD in 200 ml of Pb (II) solutions having initial concentration 10 ppm and the pH values were maintained within the range 2 – 8. It was observed that with rise in pH, the Q_e and R% values increased gradually, reached a maximum, and then declined marginally as the pH increased further. The optimum Pb (II) uptake occurred at pH = 6, with Q_e = 14.56 mg/g and R% = 72.8%. In order to realize the surface charge over CD, the point of zero charge was determined as pH_{pzc} = 5.0, according to the standard methodology described in previous studies (Kumari *et al*., 2015; Rajput *et al*., 2016). At lower pH the Pb (II) ions compete with H^+ ions to bind with the available active sites. Additionally, at pH < pH_{pzc} the adsorbent surface acquired an overall positive charge, thus repelling Pb (II) ions. However, the surface attained a negative charge at pH > pH_{pzc}, luring Pb (II) ions to bind with the active sites. A marginal reduction in the values of Q_e and R% at pH 7 and 8 may be attributed to formation of lead hydroxide, thereby resulting in decreased adsorption (Gundogdu *et al*., 2009; Chakravarty *et al*., 2010).

In order to study the effect of adsorbent dose, batch experiments were carried out separately using 0.05 – 0.25 g of CD in 200 ml of 10 ppm Pb (II) solution maintained at optimum pH = 6. The adsorption capacity initially increased, attained a maximum value at adsorbent dose 0.1 g, then it decreased gradually with further increase in adsorbent dose. The initial rise in Q_e with

increase in adsorbent dosage might be attributed to an increased availability of binding sites. However, at higher adsorbent doses, a consistent decrease in Q_e was observed which might be explained by the self – binding property of the adsorbent material, causing formation of large sized aggregates (Nuhoglu & Malkoc, 2009; Iqbal *et al*., 2016). The R% values also exhibited similar pattern of variation. Consequently, 0.1 g was deemed as the optimal adsorbent dosage for the experiments.

For examining the kinetics of Pb (II) adsorption, batch experiments were performed utilizing 0.1 g of CD in 200 ml of 10 ppm Pb (II) solution, maintained at pH = 6 for contact time durations of 30 – 240 minutes at 298 K temperature. It is evident from data, that with increase in contact time, Q_t initially rose sharply, then gradually slowed and eventually reached a constant equilibrium value. The adsorption equilibrium was attained within 240 mins. As shown in **Figure 4**, the acquired data was evaluated using pseudo-first order, second order and Weber Morris. The obtained kinetic parameters have been illustrated in **Table 1**.

The pseudo first order model is predicated on the idea that the adsorption process is reversible and the rate is governed by the initially available active surface sites. However, with increasing surface coverage, the adsorption rate declines exponentially. The mathematical equation below may be employed to formulate this model (Reddy *et al*., 2010):

$$\log(Q_e - Q_t) = \log Q_e - \frac{k_1 . t}{2.303}$$

In this equation, Q_e and Q_t represent the uptake capacities (mg/g) at equilibrium and time t respectively, while k_1 is the rate constant (min^{-1}). Plotting log (Q_e – Q_t) versus t yielded the kinetic parameters for this model. Similarly, the pseudo second order model assumes that the process is regulated by chemisorption or certain other comparably stronger forces. It may be expressed with help of following linear equation (Reddy *et al*., 2010; Ahmad *et al*., 2017):

$$\frac{t}{Q_t} = \frac{1}{k_2 . Q_e^2} + \frac{t}{Q_e}$$

where k_2 denotes the rate constant (g/mg/min). The estimation of parameters was achieved with the aid of t/Q_t versus t plot. The pseudo-second order model reliably explained the kinetics as evidenced by the close concordance between calculated equilibrium uptake capacity $Q_{e\,(calc)}$ = 14.99 mg/g and the actual experimental value $Q_{e\,(obs)}$ = 14.56 mg/g. This finding was also supported by the substantially high value of coefficient of determination (R^2 = 0.9998) and considerably lower value of chi – square (χ^2 = 0.1489).

The following Weber-Morris model equation can be used to explicitly reveal the general direction of the diffusion process (Gundogdu *et al*., 2009; Ahmad *et al*., 2016):

$$Q_t = k_{id} . t^{1/2} + C$$

where boundary layer thickness is designated by C, and the rate constant by k_{id} ($mg/g/min^{1/2}$). The actual diffusion mechanism involved may be visualized by Q_t versus $t^{1/2}$ plot. A graph with multi-linear plot typically reveals that the process incorporates numerous diffusion pathways. Similarly, a straight-line graph passing through the origin reflects that intraparticle diffusion is fully responsible for controlling the process (Arris *et al*., 2016). As evident from the figure, the plot of Q_t versus $t^{1/2}$ was noticeably linear with R^2 value = 0.9412. However, major divergence of intercept C from origin demonstrated that surface sorption was a major factor in the diffusion process in addition to pore diffusion (Arris *et al*., 2016).

Adsorption isotherm study was performed using 0.1 g CD in 200 ml of 10 – 250 ppm Pb (II) solutions, each maintained at pH = 6. It was observed that with rise in initial Pb (II) concentration, the Q_e value gradually increased till it reached a nearly constant value, however

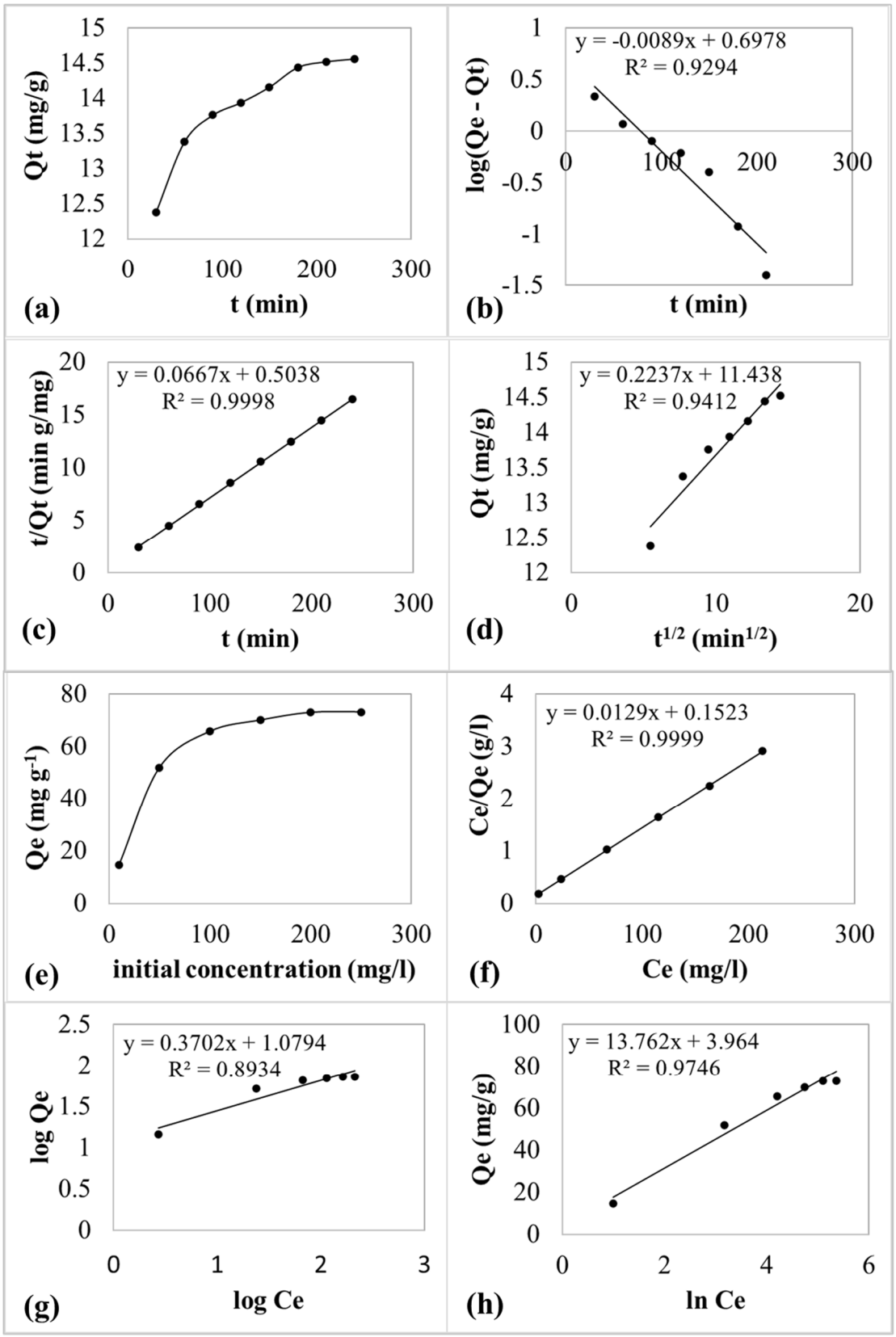

Fig. 4. (a) Effect of contact time on adsorption capacity; (b) Pseudo first order kinetics; (c) Pseudo second order kinetics; (d) Intraparticle diffusion; (e) Effect of Pb (II) ion concentration on adsorption capacity and (f) Langmuir (g) Freundlich (h) Temkin isotherms

Table 1. Parameters for adsorption kinetics, isotherms and thermodynamics

Adsorption Kinetics		**Adsorption Isotherms**	
Pseudo-first order		***Langmuir isotherm***	
$Q_{e\ (obs)}$ (mg/g)	14.56	Q_m (mg/g)	77.52
$Q_{e\ (calc)}$ (mg/g)	4.98	b (l/mg)	0.08
k_1 (min^{-1})	0.02	R_L	0.54
R^2	0.9294	R^2	0.9999
χ^2	5.9898	χ^2	0.0094
Pseudo-second order		***Freundlich isotherm***	
$Q_{e\ (obs)}$ (mg/g)	14.56	K_F (mg/g)	12.01
$Q_{e\ (calc)}$ (mg/g)	14.99	n (g/l)	2.70
k_2 (g/mg/min)	0.01	R^2	0.8934
R^2	0.9998	χ^2	8.9365
χ^2	0.1489		
Intraparticle diffusion		***Temkin isotherm***	
k_{id} (mg/g/$min^{1/2}$)	0.22	b_T	180.03
C (mg/g)	11.44	K_T (l/mg)	1.33
R^2	0.9412	R^2	0.9746
χ^2	0.0225	χ^2	1.4782

Adsorption thermodynamics

Temperature (K)	Ce (mg/l)	C_S (mg/l)	K_C	ΔG° (kJ/mol)	ΔH° (kJ/mol)	ΔS° (kJ/K/mol)
288	2.89	7.11	2.46	-2.15		
298	2.72	7.28	2.67	-2.44	8.08	0.03
308	2.46	7.54	3.06	-2.87		

the R% values exhibited a completely opposite pattern and decreased regularly with increase in initial Pb (II) concentration. The obtained isotherm data was fitted to Langmuir, Freundlich and Temkin isotherm models as shown in **Figure 4** and the obtained isotherm parameters have been listed in **Table 1**. The Langmuir adsorption isotherm is based on the idea that the adsorption process takes place at energetically equivalent active sites. This approach is mainly useful for explaining monolayer adsorption, in which the Pb (II) ions adhered to the adsorbent surface form a single layer. The linear form of this isotherm mode may be expressed as (Gundogdu *et al*., 2009):

$$\frac{C_e}{Q_e} = \frac{1}{b.Q_m} + \frac{C_e}{Q_m}$$

where C_e represents the equilibrium concentration of Pb (II) ions in the solution (mg/l). Q_m equals the maximum monolayer uptake capacity (mg/g) and Q_e signifies the amount of Pb (II) adsorbed per unit mass of adsorbent (mg/g) at equilibrium. The affinity of CD towards Pb (II) ions may be indicated by the constant "b". These parameters were computed utilising the C_e/Q_e versus C_e plot. The suitability of the process may also be defined by the dimensionless factor R_L (Chakravarty *et al*., 2010):

$$R_L = \frac{1}{1 + b.C_0}$$

where C_0 is the initial Pb (II) concentration (mg/l). A value of R_L between 0 and 1 indicates the process to be favourable, whereas values 1, 0, and R_L >1 typically imply linear, irreversible, or unfavourable nature of the process. The Freundlich isotherm model describes adsorption

over a surface having heterogenous energy distribution, leading to formation of several layers rather than just one monolayer. This mode is particularly useful when the Langmuir model's requirements of uniform, monolayer adsorption are violated. The approach of this model may be stated in the form of following equation (Abdel-Aty *et al*., 2013):

$$\log Q_e = \log K_F + \frac{1}{n} \log C_e$$

where K_F and n are the constants which may be associated with the affinity of the adsorbent towards Pb (II) ions. The parameters of this model were estimated with help of the plot log Q_e versus log C_e. The model's viability may be expressed by the value of constraint 'n', which should be between 1 and 10.

In contrast to Langmuir and Freundlich models, the Temkin isotherm emphasizes on the variation in heat of adsorption with surface coverage. It assumes that the adsorbate-adsorbent interactions cause linear decrease of heat of adsorption with surface coverage. The linear form of the model may be expressed by following equation (Ahmad *et al*., 2017; Medhi *et al*., 2020):

$$Q_e = \frac{RT}{b_T} \ln K_T + \frac{RT}{b_T} \ln C_e$$

where the constants T and R represent the absolute temperature and the gas constant respectively. Similarly, b_T and K_T are constants having units J mol^{-1} and L g^{-1} respectively. The constant b_T reveals the strength of interaction between Pb (II) ions and adsorbent. The endothermic nature of adsorption may be indicated by positive values of b_T, while the $b_T < 0$ confirms the exothermic nature the process. The plot Q_e versus ln C_e was employed to ascertain the respective parameters.

The isotherm data for adsorption of Pb (II) over CD best fitted with the Langmuir model (R^2 = 0.9999) followed by Temkin (R^2 = 0.9746) and Freundlich (R^2 = 0.8934) models respectively. This trend was also corroborated by the lowest $\chi 2$ value observed for the Langmuir model ($\chi 2$ = 0.0094) followed by Temkin ($\chi 2$ = 1.4782) and Freundlich ($\chi 2$ = 8.9365) models. As a result, Pb (II) adsorption over CD was preferentially monolayered, with a maximum monolayer capacity Q_m = 77.52 mg/g. However, the significance of the Temkin model ($R^2 > 0.9$) cannot be overlooked, indicating that to an extent, adsorption also involved formation of multilayers. The separation factor $0 < R_L < 1$ and the Freundlich constant $n > 1$ indicating that the adsorption process was favourable. The Temkin constant b_T was substantially greater than 0, suggesting that the adsorption was endothermic.

Batch experiments were performed in an incubator maintained at 288, 298 and 308 K temperatures so as to explore the effect of temperature on the process. The enthalpy change (ΔH°), entropy change (ΔS°) and the free energy change (ΔG°) accompanying the adsorption process were computed with help of Vant Hoff plot between ln K_C and 1/T shown in **Figure 5**. The corresponding parameters have been listed in **Table 1**.

The Vant Hoff equation is usually expressed by following equations (Siddiqui, 2018; Park & Lee, 2020):

$$K_C = \frac{C_s}{C_e} = \frac{C_0 - C_e}{C_e}$$

$$\ln K_C = \frac{-\Delta H^0}{RT} + \frac{\Delta S^0}{R}$$

K_C is the dimensionless equilibrium constant; R is the gas constant having value 8.314 J/K/

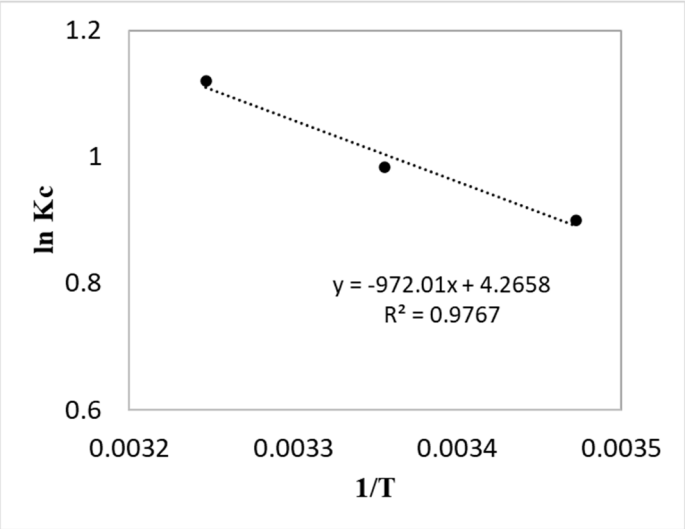

Fig. 5. Vant Hoff plot for adsorption of Pb (II) ions over CD

mol and T is the absolute temperature. C_0 denotes the initial Pb (II) concentration (mg/l), C_e is the equilibrium Pb (II) concentration in the supernatant phase (mg/l), while C_s represents the equilibrium Pb (II) concentration in the solid phase (mg/l). Similarly, ΔG^0 may be evaluated as follows (Hasan *et al*., 2019 a):

$$\Delta G = -RT \ln K_C$$

Positive values for enthalpy change ($\Delta H° = 8.08$ kJ/mol) confirmed the endothermic nature of the adsorption process. Moreover, since $\Delta H° < 40$ kJ/mol, the mechanism of adsorption was expected to be physisorption **(**Kumari *et al*., 2020; Salawu *et al*., 2022). Similarly, the parameters $\Delta G° < 0$ and $\Delta S° > 0$, suggest spontaneous nature and considerable haphazardness at the liquid – solid interface (Sahmoune, 2019).

The adsorption capacities of various tree bark adsorbents used in the literature for the adsorptive removal of Pb (II) ions have been compared in **Table 2**. The discrepancies in experimental conditions frequently render comparison of adsorbents exceedingly difficult. Therefore, in order to simplify the comparison usually the Langmuir maximum monolayer uptake capacity (Q_m) is utilized. The present study demonstrates that at pH 6.0 and 25°C temperature, using 0.5 g/l dose of *Cedrus deodara* tree bark resulted in achieving $Q_m = 77.52$ mg/g, which was certainly higher than most of the other adsorbents reported in literature.

MLR model was attempted to formulate the mathematical expression describing the dependence of Pb (II) removal efficiency (R%) on various predictor variables such as pH, adsorbent dosage (g), contact time (min), initial concentration (mg/l), and temperature (°C). **Figure 6 (a)** depicts the Pareto chart of standardised effects, which provides an insightful visual overview of the key predictors. Considering 5 predictor variables, with 25 data points and degrees of freedom (df) = 19, the statistical significance of predictor variables at significance level (α) = 0.05 was determined by critical t-value = 2.093. As evident from the figure, among the predictor variables, initial Pb (II) concentration, pH and adsorbent dose emerged as statistically significant contributors in predicting the removal efficiency (R%). **Figure 6 (b)** depict the normal probability (P-P) plot of the standardized residuals of MLR model. The obtained residuals were standardized by scaling them based on their standard deviation. As evident from the figure, the points appear to form a reasonably straight line suggesting that the standardized residuals were

Table 2. Comparison of maximum monolayer adsorption capacities (Q_m) of various tree barks reported for removal of Pb (II) ions.

Tree bark	pH	Adsorbent dose (g/l)	Q_m (mg/g)	Reference
Pinus nigra	8	2.5	49.00	**Argun & Dursun, 2007**
Neem	5	7.5	83.33	**Naiya *et al.*, 2008**
Pinus brutia	4	1.0	76.80	**Gundogdu *et al.*, 2009**
Moringa oleifera	5	4	34.60	**Reddy *et al.*, 2010**
Pinus elliottii	5	10	12.42	**Junior *et al.*, 2012**
Metroxylon sago	5	-	31.44	**Fauzia *et al.*, 2018**
Prosopis juliflora	5	0.3	27.47	**Gayathri *et al.*, 2018**
Schleichera oleosa	6	10	69.44	**Khatoon *et al.*, 2018**
Grape vine	4.5	0.5	91.00	**Haydar *et al.*, 2020**
Cedrus deodara	**6**	**0.5**	**77.52**	**Present study**

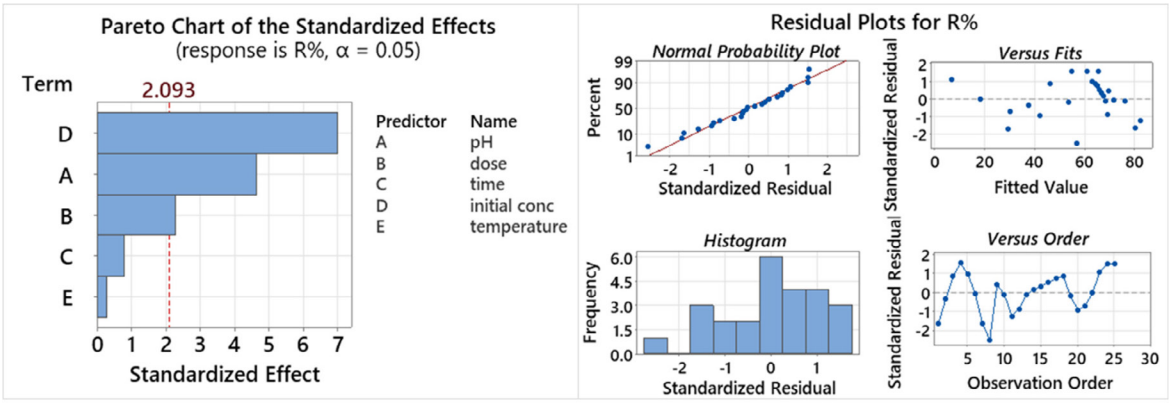

(a) **(b)**

Fig. 6. (a) Pareto chart of standardized effects and (b) standardized residual plots for MLR model.

normally distributed.

The overall model summary, results of the ANOVA analysis and corresponding values of the coefficients obtained for MLR model have been illustrated in **Table 3**. The model exhibited R^2 value = 0.8170 and R^2 (Adj.) value = 0.7689 with standard estimate of error (S) = 10.2567. The ANOVA results indicated that the MLR model significantly explained the variance in response variable ($p < 0.01$). Moreover, pH, adsorbent dose and initial Pb (II) concentration appeared to be statistically significantly decisive factors in the adsorption process ($p < 0.01$). This observation further supported the findings of Pareto chart. With help of the coefficients, it may be pointed out that following linear mathematical equation may be employed to compute Pb (II) removal efficiency:

$$R\% = -56 + 8.48*pH + 128.2*dose - 0.0277*time - 0.2356*concentration + 0.215*temperature$$

When compared to MLR, the Artificial Neural Networks (ANNs) give better flexibility in data modeling because, unlike MLR, ANNs are capable of identifying non-linear relationships and can also cope with complicated multidimensional and incomplete data (Kareem & Pathak, 2016). Studies suggest that ANNs are potentially valuable in modelling experimental data related to environmental contamination particularly concerning the water treatment (Fiyadha *et al.*, 2023). The present study utilizes ANN for modelling the adsorption process and predicting

Table 3. Details of MLR model

MODEL SUMMARY					
		R^2	Adj R^2	Pred R^2	S
		0.8170	0.7689	0.5785	10.2567
ANOVA RESULTS					
Source	***df***	***Adj SS***	***Adj MS***	***F-value***	***p-value***
Regression	5	8924.1	1784.82	16.97	0.000
pH	1	2260.8	2260.77	21.49	0.000
dose	1	543.0	543.02	5.16	0.035
time	1	66.6	66.65	0.63	0.436
initial conc	1	5161.2	5161.17	49.06	0.000
temperature	1	9.2	9.25	0.09	0.770
Error	19	1998.8	105.20		
Total	24	10922.9			
COEFFICIENTS					
Term	***Coef***	***SE Coef***	***T-value***	***p-value***	***VIF***
Constant	-56	217	-0.26	0.800	
pH	8.48	1.83	4.64	0.000	1.05
dose	128.2	56.4	2.27	0.035	1.06
time	-0.0277	0.0348	-0.80	0.436	1.13
initial conc	-0.2356	0.0336	-7.00	0.000	1.11
temperature	0.215	0.725	0.30	0.770	1.00

the Pb (II) removal efficiency (R%) based on experimental data acquired from batch adsorption study using *Cedrus deodara* bark powder as adsorbent.

The ANN architecture comprised of three layers: one input layer, one hidden layer, and one output layer. The input layer receives input data from 5 nodes corresponding to the input variables pH, adsorbent dosage, contact time, initial concentration and temperature. The hidden layer acts as the network's processing core, where it establishes complex correlations between input data and the target variable (R%). Each of the hidden layer neurons contributed in inducing non-linearity into the model by applying tangent sigmoid (*tansig*) activation to the weighted sum of inputs. This non-linearity allowed the network to recognize intricate relationships and dependencies in the data that a linear model could overlook. The output layer consisted of a single node, representing the predicted removal efficiency (R%). The output node employed pure linear (*purelin*) activation, ensuring that the final prediction is a continuous value, making it suitable for regression applications.

Levenberg-Marquardt algorithm was implemented for training the model as it can manage non-linear relationships and is resistant to outliers in data (Wilamowski & Yu, 2010). The experimental data set was randomly split into usually prescribed ratios 70:15:15 i.e., 70% for training, 15% for validation and an additional 15% for testing (Genc & Tunc, 2019). The ANN architecture was further improved by optimizing the number of neurons in the hidden layer. Underfitting might occur if there are too few neurons, resulting in inaccurate predictions. Similarly, overfitting may occur when the model retains the training data and fails to apply it to new, unknown data.

Figure 7 (a) displays the variation of mean squared error (MSE) with change in number of neurons in the hidden layer. It is evident from the figure that using 10 neurons in the hidden layer reduces MSE for both training (0.0282) and validation (2.6064) sets. As a result, neural network with 10 neurons in the hidden layer was deemed optimal for prediction, with schematic representation and architecture illustrated in **Figure 7 (b)**. The values of weights and biases used in different layer based on the optimum ANN structure have been illustrated in **Table 4** (Hasan *et al*., 2019 b).

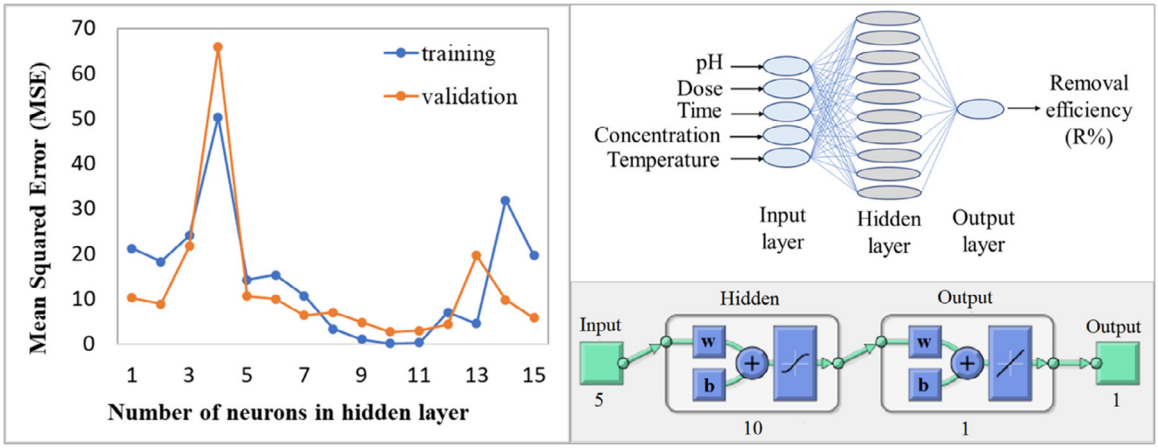

Fig. 7. (a) Variation of mean squared error (MSE) with number of neurons in the hidden layer and (b) Structure of optimal ANN model

Table 4. The weights and biases of the trained ANN*

w1	w2	b1	b2
[1.0468 -3.8872 0.22754 2.4442 -0.43868;	[-1.3959 0.45923	[-1.7651;	[-0.13695]
0.83441 0.65871 -2.6825 -0.61522 -0.29932;	0.39953 0.48086	-2.3276;	
-0.86892 1.5824 1.2391 -1.5 0.77101;	-1.5364 -1.2305	1.5466;	
0.56665 -0.17625 2.2869 -1.3698 0.85603;	0.54154 0.17909	-0.5745;	
-0.13045 0.86659 -0.05047 -3.938 -1.108;	0.74821 -0.4037]	-0.7399;	
-2.2423 -0.48397 0.52462 2.8691 0.37893;		1.5138;	
-1.8848 -1.7195 0.96549 0.40176 0.098135;		-1.5525;	
-0.35999 0.74464 -3.5208 0.45822 0.57018;		-0.076846;	
2.2216 0.78178 1.4124 0.7111 0.64283;		2.0836;	
0.78683 0.84499 -0.44289 -1.2388 0.60955]		2.6009]	

**w1 = weight matrix for connections between input layer and hidden layer.*
w2 = weight matrix for connections between hidden layer and output layer
b1 = bias vector associated with hidden layer.
b2 = bias vector associated with output layer.

The performance validation of the ANN model is crucial for ensuring that its accuracy extends well beyond the training data, generating trustworthy predictions for fresh, previously unknown samples. The performance of ANN model was validated by comparing MSE with successive iterations as depicted in **Figure 8**. As evident from the figure, each subsequent iterations resulted in regular decrease in MSE for training, validation and testing sets. However, as the number of iterations further increased, the network eventually started over-fitting the data, causing slight increase in the error. It was observed that best results were obtained at 10^{th} iteration of the network. The corresponding regression plots for training, validation and testing have been shown in **Figure 9**. The regression coefficients (R) obtained for training (0.99997), validation (0.9992) and testing data (0.9915) were > 0.99, suggesting that ANN model fitted well with the adsorption data.

Figure 10 (a) shows a comparison between the experimentally observed values of removal efficiency (R%) and those predicted through MLR and ANN models for each individual observation. It may be easily observed from figure that ANN model provides a far better prediction with each predicted value almost overlapping the experimentally observed values. A scatterplot of predicted versus experimental R% values has been displayed in **Figure 10 (b)**.

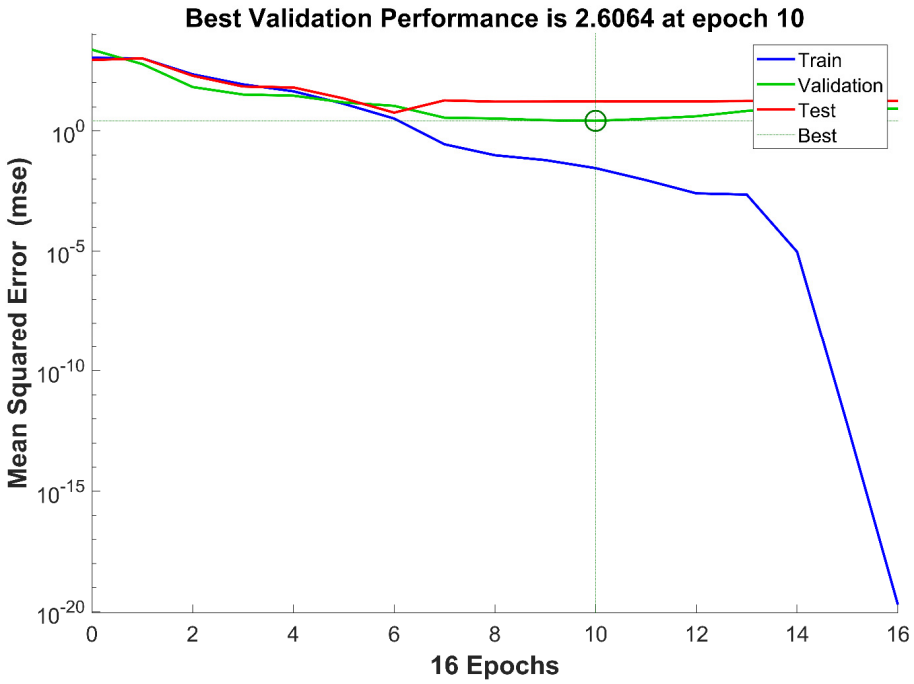

Fig. 8. Validation performance of the ANN model

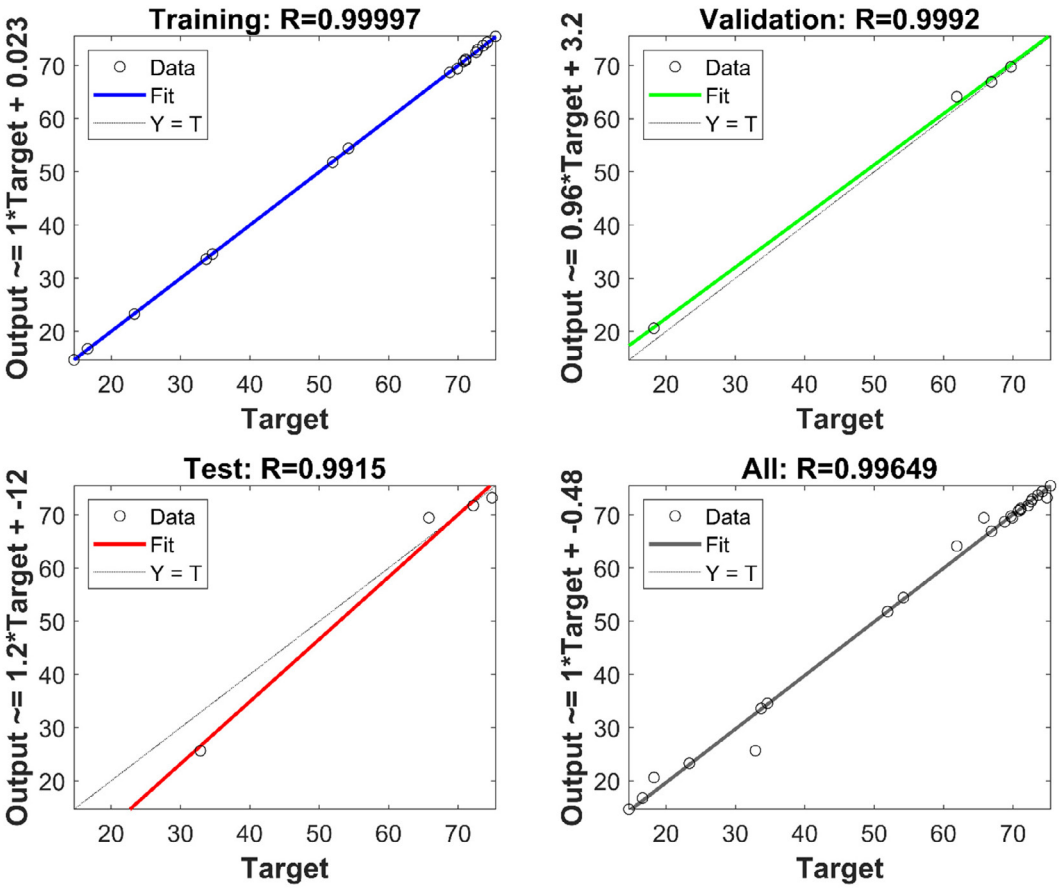

Fig. 9. Regression plots for training, validation and testing of ANN model

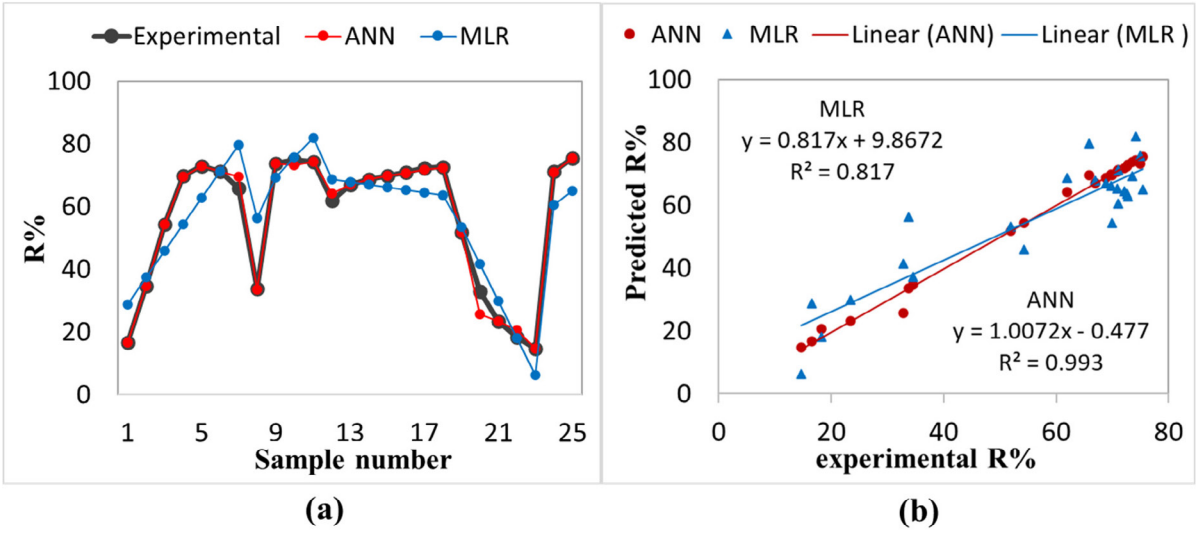

Fig. 10. (a) Prediction of removal efficiency (R%) using MLR and ANN and (b) Plot of predicted and experimentally observed values of R%

Table 5. Statistical comparison of MLR and ANN models

	R^2	RMSE	MAPE (%)
MLR	0.817	8.954	17.379
ANN	0.993	1.777	2.054

The overall accuracy of MLR and ANN models may be statistically evaluated in terms of RMSE, MAPE and R^2 values as shown in **Table 5**.

As indicated by significantly low values of RMSE (1.777), MAPE (2.054%) and relatively higher R^2 value (0.993) for ANN model, it may be inferred that ANN model may serve as a useful tool for modelling adsorption and predicting removal efficiency based on the key predictors pH, adsorbent dose, contact time, initial concentration and temperature.

CONCLUSION

This study reveals a novel and environmentally significant technique for removing Pb (II) ions from water by utilizing *Cedrus deodara* tree bark, which is a non-toxic waste product from timber industry. Since the obtained maximum uptake capacity (Q_m) exceeded several other reported adsorbents, the use of *Cedrus deodara* tree bark powder (CD) as an adsorbent offers an affordable, environmentally friendly, and green solution for purification of water. Additionally, the effective implementation of an Artificial Neural Network (ANN) model reveals the relevance of modern computational tools in exploring adsorption processes, paving the way for future environmental research and remediation. The study demonstrated that treating 200 ml of 10 ppm Pb (II) solution maintained at pH = 6 with 0.1 g of CD resulted in achieving equilibrium uptake capacity (Q_e) = 14.56 mg/g and removal efficiency (R%) = 72.8. The experimental data fitted well with pseudo-second order kinetic model and the Langmuir isotherm model. Similarly, the solute diffusion was impacted by both surface and pore diffusion processes. The thermodynamic parameters revealed endothermic and spontaneous nature of the adsorption. Considering pH, adsorbent dosage, contact time, initial concentration and temperature as factors,

MLR and ANN models were formulated for prediction of Pb (II) removal efficiency (R%). A statistical comparison utilizing R^2, RMSE and MAPE values revealed that, as compared to the MLR model, the ANN model predicted removal efficiency with greater accuracy.

ACKNOWLEDGEMENT

We are grateful to the Chemistry Department, Sam Higginbottom University of Agriculture, Technology, and Sciences, Prayagraj, India, for generously supplying us with the necessary facilities. We would also sincerely acknowledge and thank Dr. Nishant Ranjan, Assistant Professor, UCRD, Chandigarh University, Mohali, India and Mr. Manish Kumar Pandey, Analytical Division, Biotech Park, Lucknow, U.P., India for their invaluable technical support during analysis of the samples.

GRANT SUPPORT DETAILS

The present research did not receive any financial support.

CONFLICT OF INTEREST

The authors declare that there is no conflict of interest regarding the publication of this manuscript. In addition, the ethical issues, including plagiarism, informed consent, misconduct, data fabrication and/ or falsification, double publication and/or submission, and redundancy has been completely observed by the authors.

LIFE SCIENCE REPORTING

No life science threat was practiced in this research.

REFERENCES

Abdel-Aty, A. M., Ammar, N. S., Ghafar, H. H. A., & Ali, R. K. (2013). Biosorption of cadmium and lead from aqueous solution by fresh water alga *Anabaena sphaerica* biomass. Journal of advanced research, 4(4); 367-374.

Ahmad, R., & Hasan, I. (2016). L-cystein modified bentonite-cellulose nanocomposite (cellu/cys-bent) for adsorption of Cu^{2+}, Pb^{2+}, and Cd^{2+} ions from aqueous solution. Separation science and technology, 51(3); 381-394.

Ahmad, R., & Hasan, I. (2017). L-methionine montmorillonite encapsulated guar gum-g-polyacrylonitrile copolymer hybrid nanocomposite for removal of heavy metals. Groundwater for Sustainable Development, 5; 75-84.

Argun, M. E., & Dursun, S. (2007). Activation of pine bark surface with NaOH for lead removal. J Int Environ Appl Sci, 2; 5-10.

Arris, S., Lehocine, M. B. & Meniai, A. H. (2016). Sorption study of chromium sorption from wastewater using cereal by-products. International Journal of Hydrogen Energy, 41(24); 10299-10310.

ATSDR (2019). ATSDR's substance priority list. Agency for Toxic Substances and Disease Registry. Accessible at https://www.atsdr.cdc.gov/spl

Banerjee, S., Kumar, A., Maiti, S. K., & Chowdhury, A. (2016). Seasonal variation in heavy metal contaminations in water and sediments of Jamshedpur stretch of Subarnarekha river, India. Environmental Earth Sciences, 75(3); 1-12.

Barakat, M. A. (2011). New trends in removing heavy metals from industrial wastewater. Arabian Journal of Chemistry, 4(4); 361-377.

Capobianco, G., Pelosi, C., Agresti, G., Bonifazi, G., Santamaria, U., & Serranti, S. (2018). X-ray fluorescence investigation on yellow pigments based on lead, tin and antimony through the

comparison between laboratory and portable instruments. Journal of Cultural Heritage, 29; 19-29.
Carolin, C. F., Kumar, P. S., Saravanan, A., Joshiba, G. J., & Naushad, M. (2017). Efficient techniques for the removal of toxic heavy metals from aquatic environment: A review. Journal of Environmental Chemical Engineering, 5(3); 2782-2799.
Chakravarty, P., Sarma, N. S., & Sarma, H. P. (2010). Removal of lead (II) from aqueous solution using heartwood of *Areca catechu* powder. Desalination, 256(1-3); 16-21.
Ciesielczyk, F., Bartczak, P., Wieszczycka, K., Siwińska-Stefańska, K., Nowacka, M., & Jesionowski, T. (2013). Adsorption of Ni (II) from model solutions using co-precipitated inorganic oxides. Adsorption, 19(2); 423-434.
Coates, J. (2000). Interpretation of infrared spectra, a practical approach. Encyclopedia of Analytical Chemistry, R.A. Meyers (Ed.) John Wiley & Sons Ltd. pp. 10815–10837.
CWC (Central Water Commission). (2019). Status of trace & toxic metals in Indian rivers. Ministry of Jal Shakti, Department of Water Resources, River Development and Ganga Rejuvenation: New Delhi, India. Accessible at: http://cwc.gov.in/sites/default/files/status-trace-toxic-metals-indian-rivers-2019-2.pdf
Das, R., Mukherjee, A., Sinha, I., Roy, K., & Dutta, B. K. (2020). Synthesis of potential bio-adsorbent from Indian Neem leaves (*Azadirachta indica*) and its optimization for malachite green dye removal from industrial wastes using response surface methodology: kinetics, isotherms and thermodynamic studies. Applied Water Science, 10(5); 1-18.
Fauzia, S., Aziz, H., Dahlan, D., & Zein, R. (2018). Study of equilibrium, kinetic and thermodynamic for removal of Pb (II) in aqueous solution using Sago bark (*Metroxylon sago*). In AIP Conference Proceedings (Vol. 2023, No. 1). AIP Publishing. https://doi.org/10.1063/1.5064078.
Fiyadha, S. S., Alardhi, S. M., Al Omar, M., Aljumaily, M. M., Al Saadic, M. A., Fayaedd, S. S., ... & El-Shafie, A. (2023). A comprehensive review on modelling the adsorption process for heavy metal removal from water using artificial neural network technique. Heliyon, 9; e15455.
Fomina, M., & Gadd, G. M. (2014). Biosorption: current perspectives on concept, definition and application. Bioresource Technology, 160; 3-14.
Fuks, L., Filipiuk, D. & Majdan, M. (2006). Transition metal complexes with alginate biosorbent. Journal of Molecular Structure, 792; 104-109.
Gayathri, N.S., Anuradha, J., & Andal, N. M. (2018). Efficacy of modified tree bark in the screening of divalent ions in aqueous media: characterization and isothermal studies. International Journal of Current Engineering and Scientific Research, 5(4); 127-132.
Genc, B., & Tunc, H. (2019). Optimal training and test sets design for machine learning. Turkish Journal of Electrical Engineering and Computer Sciences, 27(2); 1534-1545.
Grover, M. (2021). An Overview on the Ornamental Coniferous Tree *Cedrus deodara* (Roxburgh) G. Don (Himalayan Cedar). Journal of Ayurveda and Integrated Medical Sciences, 6(4); 291-302.
Gundogdu, A., Ozdes, D., Duran, C., Bulut, V. N., Soylak, M., & Senturk, H. B. (2009). Biosorption of Pb (II) ions from aqueous solution by pine bark (*Pinus brutia Ten*.). Chemical Engineering Journal, 153(1-3); 62-69.
Gupta, G. K., & Mondal, M. K. (2020). Mechanism of Cr (VI) uptake onto sagwan sawdust derived biochar and statistical optimization via response surface methodology. Biomass Conversion and Biorefinery, 2020; 1-17.
Hafizoglu, H., & Holmbom, B. (1987). Studies on the chemistry of *Cedrus libani* A. Rich. II: Lipophilic constituents of the cedar bark. Holzforschung, 41(2); 73-77.
Hallinan, J. S. (2013). Computational intelligence in the design of synthetic microbial genetic systems. In Methods in microbiology. Academic Press. Vol. 40, pp. 1-37.
Haydar, S., Farooq, M. U., & Gull, S. (2020). Use of grape vine bark as an effective biosorbent for the removal of heavy metals (copper and lead) from aqueous solutions. Desalination and Water Treatment, 183; 307-314.
Hwang, K., Kwon, G. J., Yang, J., Kim, M., Hwang, W. J., Youe, W., & Kim, D. Y. (2018). *Chlamydomonas angulosa* (Green Alga) and *Nostoc commune* (Blue-Green Alga) microalgae-cellulose composite aerogel beads: manufacture, physicochemical characterization, and Cd (II) adsorption. Materials, 11(4); 562.
Ijomah, M. N. C., & Okoyeh, F. N. (1988). Microstructure and deformation resistance of quinary Pb-(Al, Mg, Sn, Li) alloys. Metallography, 21(2); 165-178.
Iqbal, M., Iqbal, N., Bhatti, I. A., Ahmad, N., & Zahid, M. (2016). Response surface methodology

application in optimization of cadmium adsorption by shoe waste: A good option of waste mitigation by waste. Ecological Engineering, 88; 265-275.

Jain, S., Jain, A., Jain, S., Malviya, N., Jain, V., & Kumar, D. (2015). Estimation of total phenolic, tannins, and flavonoid contents and antioxidant activity of *Cedrus deodara* heart wood extracts. Egyptian Pharmaceutical Journal, 14(1); 10.

Junior, A. C. G., Strey, L., Lindino, C. A., Nacke, H., Schwantes, D., & Seidel, E. P. (2012). Applicability of the Pinus bark (*Pinus elliottii*) for the adsorption of toxic heavy metals from aqueous solutions. Acta Scientiarum. Technology, 34(1); 79-87.

Kareem, S. S., & Pathak, Y. (2016). Clinical Applications of Artificial Neural Networks in Pharmacokinetic Modeling. In Artificial Neural Network for Drug Design, Delivery and Disposition, Academic Press. pp. 393-405.

Khatoon, A., Uddin, M. K., & Rao, R. A. K. (2018). Adsorptive remediation of Pb (II) from aqueous media using *Schleichera oleosa* bark. Environmental Technology & Innovation, 11; 1-14.

Kulisz, M., Kujawska, J., Przysucha, B., & Cel, W. (2021). Forecasting water quality index in groundwater using artificial neural network. Energies, 14(18); 5875.

Kumar, Y., Pradhan, S., Pramanik, S., Bandyopadhyay, R., Das, D. K., & Pramanik, P., (2018). Efficient electrochemical detection of guanine, uric acid and their mixture by composite of nano-particles of lanthanides ortho-ferrite $XFeO_3$ (X= La, Gd, Pr, Dy, Sm, Ce and Tb). Journal of Electroanalytical Chemistry, 830; 95-105.

Kumar, Y., Pramanik, P., & Das, D. K. (2019). Electrochemical detection of paracetamol and dopamine molecules using nano-particles of cobalt ferrite and manganese ferrite modified with graphite. Heliyon, 5(7); e02031.

Kumar, Y., Vashistha, V. K., & Das, D. K. (2020). Synthesis of Perovskite-type NdFeO3 nanoparticles and used as electrochemical sensor for detection of paracetamol. Lett. Appl. Nanobiosci., 9; 866-869.

Kumari, M., Pittman Jr, C. U., & Mohan, D. (2015). Heavy metals [chromium (VI) and lead (II)] removal from water using mesoporous magnetite (Fe_3O_4) nanospheres. Journal of Colloid and Interface Science, 442; 120-132.

Kumari, U., Biswas, S., & Meikap, B. C. (2020). Defluoridation characteristics of a novel adsorbent developed from ferroalloy electric arc furnace slag: Batch, column study and treatment of industrial wastewater. Environmental Technology & Innovation, 18; 100782.

Lee, S., & Choi, W. S. (2013). A multi-industry bankruptcy prediction model using back-propagation neural network and multivariate discriminant analysis. Expert Systems with Applications, 40(8); 2941-2946.

Liang, S., Guo, X., Lautner, S., & Saake, B. (2014). Removal of hexavalent chromium by different modified spruce bark adsorbents. Journal of Wood Chemistry and Technology, 34(4); 273-290.

Liang, W., Wang, J.J., Gaston, L.A., Huang, D., Huang, H., Lei, S., Awasthi, M.K., Zhou, B., Xiao, R., Zhang, Z. (2018). Facilitative capture of As(V), Pb(II) and methylene blue from aqueous solutions with MgO hybrid sponge-like carbonaceous composite derived from sugarcane leafy trash. Journal of Environmental Management, 212; 77–87.

Litefti, K., Freire, M. S., Stitou, M., & González-Álvarez, J. (2019). Adsorption of an anionic dye (Congo red) from aqueous solutions by pine bark. Scientific Reports, 9(1); 1-11.

Medhi, H., Chowdhury, P. R., Baruah, P. D., & Bhattacharyya, K. G. (2020). Kinetics of aqueous Cu (II) biosorption onto *Thevetia peruviana* leaf powder. ACS Omega, 5(23); 13489-13502.

Mittal, A., Ahmad, R., & Hasan, I. (2016 a). Poly (methyl methacrylate)-grafted alginate/Fe_3O_4 nanocomposite: synthesis and its application for the removal of heavy metal ions. Desalination and Water Treatment, 57(42); 19820-19833.

Mittal, A., Ahmad, R., & Hasan, I. (2016 b). Biosorption of Pb^{2+}, Ni^{2+} and Cu^{2+} ions from aqueous solutions by L-cystein-modified montmorillonite-immobilized alginate nanocomposite. Desalination and Water Treatment, 57(38); 17790-17807.

Naiya, T. K., Bhattacharya, A. K., & Das, S. K. (2008). Adsorption of Pb (II) by sawdust and neem bark from aqueous solutions. Environmental Progress, 27(3); 313-328.

Nuhoglu, Y., & Malkoc, E. (2009). Thermodynamic and kinetic studies for environmentaly friendly Ni (II) biosorption using waste pomace of olive oil factory. Bioresource Technology, 100(8); 2375-2380.

Park, J. H., & Lee, J. K. (2020). Weathered Sand of Basalt as a Potential Nickel Adsorbent. Processes,

8(10); 1238.
Politi, D. & Sidiras, D. (2020). Modified spruce sawdust for sorption of hexavalent chromium in batch systems and fixed-bed columns. Molecules, 25(21); 5156.
Pradhan, S., Biswas, S., Das, D. K., Bhar, R., Bandyopadhyay, R., & Pramanik, P., (2018). An efficient electrode for simultaneous determination of guanine and adenine using nano-sized lead telluride with graphene. New Journal of Chemistry, 42(1); 564-573.
Rajput, S., Pittman Jr, C. U., & Mohan, D. (2016). Magnetic magnetite (Fe3O4) nanoparticle synthesis and applications for lead (Pb^{2+}) and chromium (Cr^{6+}) removal from water. Journal of Colloid and Interface Science, 468; 334-346.
Reddy, D. H. K., Ramana, D. K. V., Seshaiah, K., & Reddy, A. V. R. (2011). Biosorption of Ni (II) from aqueous phase by *Moringa oleifera* bark, a low cost biosorbent. Desalination, 268(1-3); 150-157.
Reddy, D. H. K., Seshaiah, K., Reddy, A. V. R., Rao, M. M., & Wang, M. C. (2010). Biosorption of Pb^{2+} from aqueous solutions by *Moringa oleifera* bark: equilibrium and kinetic studies. Journal of Hazardous Materials, 174(1-3); 831-838.
Sahmoune, M. N. (2019). Evaluation of thermodynamic parameters for adsorption of heavy metals by green adsorbents. Environmental Chemistry Letters, 17(2); 697-704.
Salawu, O. A., Han, Z., & Adeleye, A. S. (2022). Shrimp Waste-derived Porous Carbon Adsorbent: Performance, Mechanism, and Application of Machine Learning. Journal of Hazardous Materials, 437; 129266-129271.
Sazli, M. H. (2006). A brief review of feed-forward neural networks. Communications Faculty of Sciences University of Ankara Series A2-A3 Physical Sciences and Engineering, 50(01).
Şen, A., Pereira, H., Olivella, M. A., & Villaescusa, I. (2015). Heavy metals removal in aqueous environments using bark as a biosorbent. International Journal of Environmental Science and Technology, 12(1); 391-404.
Shooto, N. D., Thabede, P. M., Bhila, B., Moloto, H., & Naidoo, E. B. (2020). Lead ions and methylene blue dye removal from aqueous solution by *Mucuna beans* (velvet beans) adsorbents. Journal of Environmental Chemical Engineering, 8(2); 103557.
Siddiqui, S. H. (2018). The removal of Cu^{2+}, Ni^{2+} and methylene blue (MB) from aqueous solution using *Luffa Actangula* carbon: kinetics, thermodynamic and isotherm and response methodology. Groundwater For Sustainable Development, 6; 141-149.
Srivastava, S., Agrawal, S. B., & Mondal, M. K. (2017). Synthesis, characterization and application of *Lagerstroemia speciosa* embedded magnetic nanoparticle for Cr (VI) adsorption from aqueous solution. Journal of Environmental Sciences, 55; 283-293.
Sud, D., Mahajan, G., & Kaur, M. P. (2008). Agricultural waste material as potential adsorbent for sequestering heavy metal ions from aqueous solutions–A review. Bioresource technology, 99(14); 6017-6027.
Syahrullah, L. O. I., & Sinaga, N. (2016). Optimization and prediction of motorcycle injection system performance with feed-forward back-propagation method Artificial Neural Network (ANN). American Journal of Engineering and Applied Science, 9(2); 222-235.
Taoufik, N., Elmchaouri, A., El Mahmoudi, S., Korili, S. A., & Gil, A. (2021). Comparative analysis study by response surface methodology and artificial neural network on salicylic acid adsorption optimization using activated carbon. Environmental Nanotechnology, Monitoring & Management, 15; 100448.
Teshager, F. M., Habtu, N. G., & Mequanint, K. (2022). A systematic study of cellulose-reactive anionic dye removal using a sustainable bioadsorbent. Chemosphere, 303; 135024.
Vazquez, G., Gonzalez-Alvarez, J., Freire, S., López-Lorenzo, M., & Antorrena, G. (2002). Removal of cadmium and mercury ions from aqueous solution by sorption on treated *Pinus pinaster* bark: kinetics and isotherms. Bioresource Technology, 82(3); 247-251.
Wilamowski, B. M. & Yu, H. (2010). Improved computation for Levenberg-Marquardt algorithm training. IEEE Transactions on Neural Network, 21 (6); 930–937.
Wu, Q., Xian, Y., He, Z., Zhang, Q., Wu, J., Yang, G., & Long, L. (2019). Adsorption characteristics of Pb (II) using biochar derived from spent mushroom substrate. Scientific Reports, 9(1); 1-11.
Xie, Y., Hu, W., Zhou, X., Yan, S., & Li, C. (2022). Artificial Neural Network Modeling for Predicting and Evaluating the Mean Radiant Temperature around Buildings on Hot Summer Days. Buildings, 12(5); 513.
Yetilmezsoy, K., & Demirel, S. (2008). Artificial neural network (ANN) approach for modeling of

Pb (II) adsorption from aqueous solution by *Antep pistachio* (*Pistacia Vera L.*) shells. Journal of hazardous materials, 153(3); 1288-1300.

Zhang, B., Han, X., Gu, P., Fang, S., & Bai, J. (2017). Response surface methodology approach for optimization of ciprofloxacin adsorption using activated carbon derived from the residue of desilicated rice husk. Journal of Molecular Liquids, 238; 316-325.